Ratchet based ion pumps for selective ion separations

Alon Herman[1], Joel W. Ager[2,3], Shane Ardo[4], and Gideon Segev[1*]

[1]School of Electrical Engineering, Tel Aviv University, 6997801, Israel

[2]Department of Materials Science and Engineering, University of California at Berkeley, Berkeley, CA, 94720, USA

[3]Materials Sciences Division, Lawrence Berkeley National Laboratory, Berkeley, CA, 94720, USA

[4]Department of Chemistry, Department of Chemical & Biomolecular Engineering, Department of Materials Science & Engineering, University of California Irvine, Irvine, CA, 92697, USA

[*]email: gideons1@tauex.tau.ac.il

The development of a highly selective, membrane-based ion separations technology could significantly improve the sustainability and energy efficiency of water treatment technologies and emerging applications such as electrochemical CO_2 reduction, extraction of valuable metals from sea water, and battery recycling. In this work we show that an electronic flashing ratchet mechanism can be used for high precision ion separation. The suggested ratchet-based ion pumps utilize a unique feature of electronic ratchets, frequency dependent current reversal, to drive ions with the same charge, but different diffusion coefficient, in opposite directions. We show that ions whose diffusion coefficients differ by as little as 1% can be separated by driving them in opposite directions with a velocity difference as high as 1.2 mm/s. Since the pumping properties of the ratchet are determined by a time-varying electric input signal, the proposed ion pumps could be instrumental in realizing an efficient, large-scale, and fit-for-purpose system for selective ion separation. Examples of ratchet-driven systems for lithium extraction from sea water, lead removal from drinking water, and water desalination are discussed and analyzed.

I. INTRODUCTION

In recent years there has been a growing demand for membranes that facilitate the extraction of a single solute from water [1–3]. The introduction of a highly selective ion separation technology could markedly advance a large variety of critical fields such as water treatment, electrochemical CO_2 reduction, resource extraction from sea water, battery recycling and many others [1–10]. For example, since reverse osmosis (RO) desalination is not selective (i.e., it rejects all ions), RO processes typically require extensive post-treatment steps or multiple passes through the RO membrane to control the concentration of specific ions at the outlet. Moreover, pre-treatment steps are also needed to minimize membrane fouling [4,6]. Thus, the addition of a highly selective membrane at different stages of desalination can greatly increase the overall energetic efficiency of the system [6]. Other examples of ion-specific separation needs include those for trace species, such as for decontamination of drinking water and wastewater, by removing heavy metal ions, or extraction of valuable metals, such as lithium, from salt water [1,4–6]. Thus, a membrane that is capable of selectively removing specific ions will be able to reduce the energy consumption of these processes, enabling the

development of new processes and technologies that are currently considered cost prohibitive.

One of the main approaches pursued for solute-solute selectivity, is filtration with sub-nanometer pore membranes. In these membranes, selectivity originates from the difference in the hydration energy between ions and the difference in their transport properties within the pores [1,2]. Despite achieving some success, highly selective separation of same-charge ions remains a fundamental challenge [1,2]. Furthermore, since these membranes rely on functionalized pores with a precise diameter below 1 nm, upscaling these membranes is a great challenge. Moreover, as the membrane selectivity is derived by the pore geometry and chemistry, different membranes must be designed for every target ion [2]. Another approach for monovalent ion separation is based on the diffusion coefficient dependent response of ions to a pressure induced streaming potential [1,11–15]. However, only a few studies have demonstrated this mechanism and so far their reported selectivity is limited.

In this work we investigate the use of an electronic flashing ratchet mechanism to separate ions with the same charge number according to their diffusion coefficients. Since the selectivity is controlled by the ratcheting process, it does not require energy intensive ion dehydration or complex sub-nanometer structures. The paper is organized as follows. First, we develop the theory, demonstrate how current reversals results in high precision separation, and find the conditions under which current reversals are possible. Next, we define the separation resolution which determines how well ions can be separated from each other. Last, we demonstrate a few use cases in which ratchet driven ion separation can improve process sustainability and efficiency.

II. FLASHING RATCHETS

Electronic flashing ratchets are devices that utilize modulation of a spatially asymmetric electric potential to drive a steady state particle flux [16–18]. The operating principle of a flashing ratchet is described schematically in Appendix B. While in most prior studies flashing rachets were used to drive electrons or holes in semiconductors [19–32], the application of flashing ratchets for ion pumping was only suggested recently. Membranes with oscillating pores for resonant osmosis were theoretically analyzed in terms of ratchet driven transport [33,34] and nanofluidic charge coupled devices, which can be viewed as reversible ratchets [35], were studied for DNA separations [36]. In a prior work, we have utilized these ratcheting principles to demonstrate experimentally a first-of-its-kind ratchet-based ion pump (RBIP) [37]. In all prior analyses [33,34,36] selectivity is achieved by transporting particles in the same direction, but at a different average velocity. However, this approach has a limited selectivity making it unfit for removing trace amounts of ions from solutions.

An important hallmark of ratchets is the ability to invert the direction of particle flow with a change in the input signal frequency [19], [38]. The frequency at which the particle's net velocity is reversed is termed the *stopping frequency*, and it is determined by the potential distribution and particle transport properties [39–41]. As a result, for a given ratchet, there can be a frequency at which particles with the same, charge but different diffusion coefficient, are transported in opposite directions. This effect has been studied theoretically [42–46], and was used to sort gold nanoparticles of different sizes and shapes [40,41,47]. However, this concept has never-before been applied to ion separations. Here we show that by utilizing velocity reversal in ratchet systems, ions with the same charge can be driven in

opposite directions according to their diffusion coefficient. This enables extraction of ions with extremely low relative concentrations if their diffusion coefficient is even slightly different from that of the majority ions in the solution. Since the direction of ion transport is determined by the input signal frequency, the sorting properties can be tuned in real time providing a simple fit-to-purpose solution for a variety of ion separations applications.

III. ANALYSIS

The response of noninteracting ions in a solution to a given potential distribution, $U(x,t)$, can be determined by the continuity equation (as described in Appendix A). The potential distribution is described as the product of spatial and temporal components:

$$U(x,t) = V(x)g(t). \qquad (1)$$

We address a one-dimensional ratchet that has an infinitely periodic sawtooth distribution in space, with a spatial period L, and is driven by a periodic square wave signal at frequency f. The spatial and temporal contributions are shown in Fig. 1, and are mathematically described by:

$$V(x) = \begin{cases} V_{max}\dfrac{x/L}{x_c}, & 0 < \dfrac{x}{L} < x_c \\ V_{max}\dfrac{(1-x/L)}{(1-x_c)}, & x_c < \dfrac{x}{L} < 1 \end{cases}, \qquad (2a)$$

$$g(t) = \begin{cases} 1, & 0 < t < \delta \cdot T \\ \alpha, & \delta \cdot T < t < T \end{cases}, \qquad (2b)$$

where V_{max} is the potential amplitude, and x_c is the spatial symmetry factor, which is the relative length of the first linear section of the sawtooth potential to the spatial period, L (see Fig. 1). The temporal modulation $g(t)$ is described by a duty-cycle $\delta = t^+/T$, which is the ratio between the time-duration of the first step, where the potential is at its maximum value, to the total period $T(=1/f)$. Each

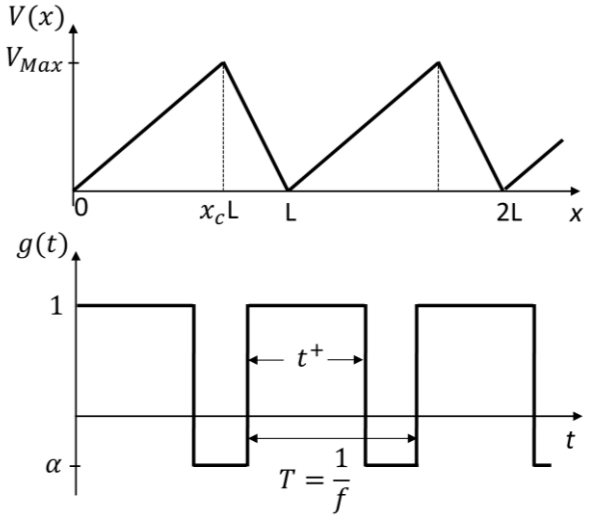

Fig. 1. The spatial and temporal components of the potential distribution.

time-period is completed with a second step, in which the sawtooth distribution is multiplied by a potential symmetry factor in the range $-1 \le \alpha \le 0$.

The continuity equation with periodic boundary conditions was solved numerically for the ion concentration, *C(x,t)*. More details on the computational model and its validation can be found in Appendixes A and C. The net ion velocity, v_{net}, is derived from the ion flux, $N(x,t)$, and is defined as the average ion velocity in space and time:

$$v_{net} = \frac{1}{TL}\int_0^T \int_0^L \frac{N(x,\tau)}{c_0}\, dx\, d\tau, \qquad (3)$$

where c_0 is the reference concentration, and $\tau = 0$ is defined to be the time at which the system enters its steady-state and the initial state of the system no longer affects its operation.

In the presented model the electric potential distribution is used as an input and Poisson's equation is not solved. Therefore, it does not consider the interactions between ions, nor the potential being screened by them. To obtain a sawtooth-like potential distribution in realistic conditions, the ratchet length scale should be small

enough, such that potential screening by the ions in the solution is not significant. This is possible if the length scale is in the order of the Debye screening length within the device. A detailed analysis of this is left for future work. Thus, this model is an ideal testcase that can help determine the optimal electric potential distribution for a given application. Unless stated otherwise, the ratchet parameters that are used in the analysis are: $L = 1\ \mu\text{m}$, $x_c = 0.7$, $V_{max} = 2.5\ \text{V}$, $\delta = 0.25$, $\alpha = -0.5$, the ion charge number is $z = 1$, the inverse thermal voltage is $\beta = 39.59\ \text{V}^{-1}$, and the reference concentration was chosen to be $c_0 = 1\ \text{mol/m}^3$. We note that since the electric potential is pre-determined, the net ion velocity is independent of c_0. Thus, the value of c_0 has no practical importance in this analysis.

IV. RESULTS

A. Velocity reversal

Ratchets can be useful for many applications, but of particular interest to us is to examine the range of parameters that drive ions with the same charge (polarity and valence), in opposite directions. The ion response to a ratchet drive was found by calculating the net ion velocity, v_{net}, for various input signals, $g(t)$, potential distributions, $V(x)$, and ions with diffusion coefficients, D. Fig. 2 illustrates a typical velocity reversal example. The figure shows the net ion velocity as a function of the ratchet signal frequency for two ions with different diffusion coefficients. For input signal frequencies between 62–103 kHz, the low D ions have a positive net velocity, and the high D ions have a negative net velocity. When the ratchet is operated at $f = 83$ kHz, the difference in net velocities is the largest. The variation of the spatially averaged ion velocity along a time-period is analysed in Appendix D. Fig. 3(a) and Fig. 3(b) show the distribution of the low D and high D ions respectively, at a few key times

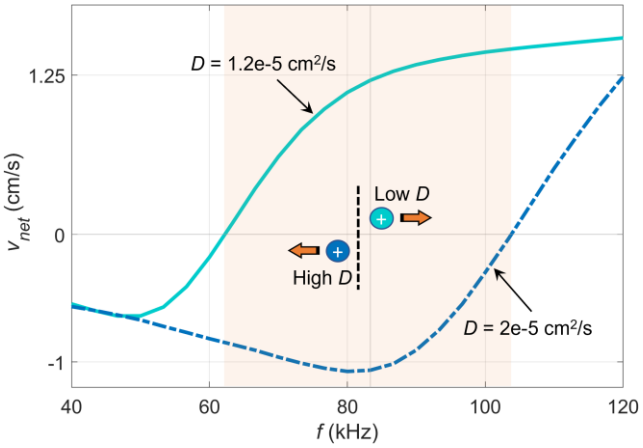

Fig. 2. The net velocity of two positively charged monovalent ions ($z = 1$), as a function of the input signal frequency. The ratchet parameters are: $L = 1\ \mu m$, $x_c = 0.7$, $V_{max} = 2.5\ V$, $\delta = 0.25$, $\alpha = -0.5$

along a time-period when the ratchet is operated at $f = 83$ kHz. Starting from $\tau = 0$, the entire ion population is crowded around the potential minima. After the first potential switch at $\tau = 0.02T$, the ion population is split into two groups drifting in opposite directions. By the time $\tau = 0.25T$, nearly all the high D ions have reached the new potential minima, while the majority of the low D ions have not. After the second potential switch, at $\tau = 0.26T$, the ions split again, but since the electric fields are lower ($\alpha = -0.5$), the groups drift apart more slowly. This allows more ions to diffuse over the potential peak and join the ions drifting in the negative x direction. When the groups are completely separated, at $\tau = 0.28T$, this process stops. The overall effect is a transfer of ions from the low field side of the sawtooth to the high field side, a phenomenon we term *injection*. An approximation of the net velocity can be made by noticing that 57% of the high D ions are traveling to the left after the first potential switch, while after the second switch only 45% return. Hence, in every time-period, about 12% of the ions are moving one spatial period in the negative direction, resulting in a net velocity of $v_{net} \approx -12\% \cdot L/T = -1\ \text{cm/s}$. In contrast, only a

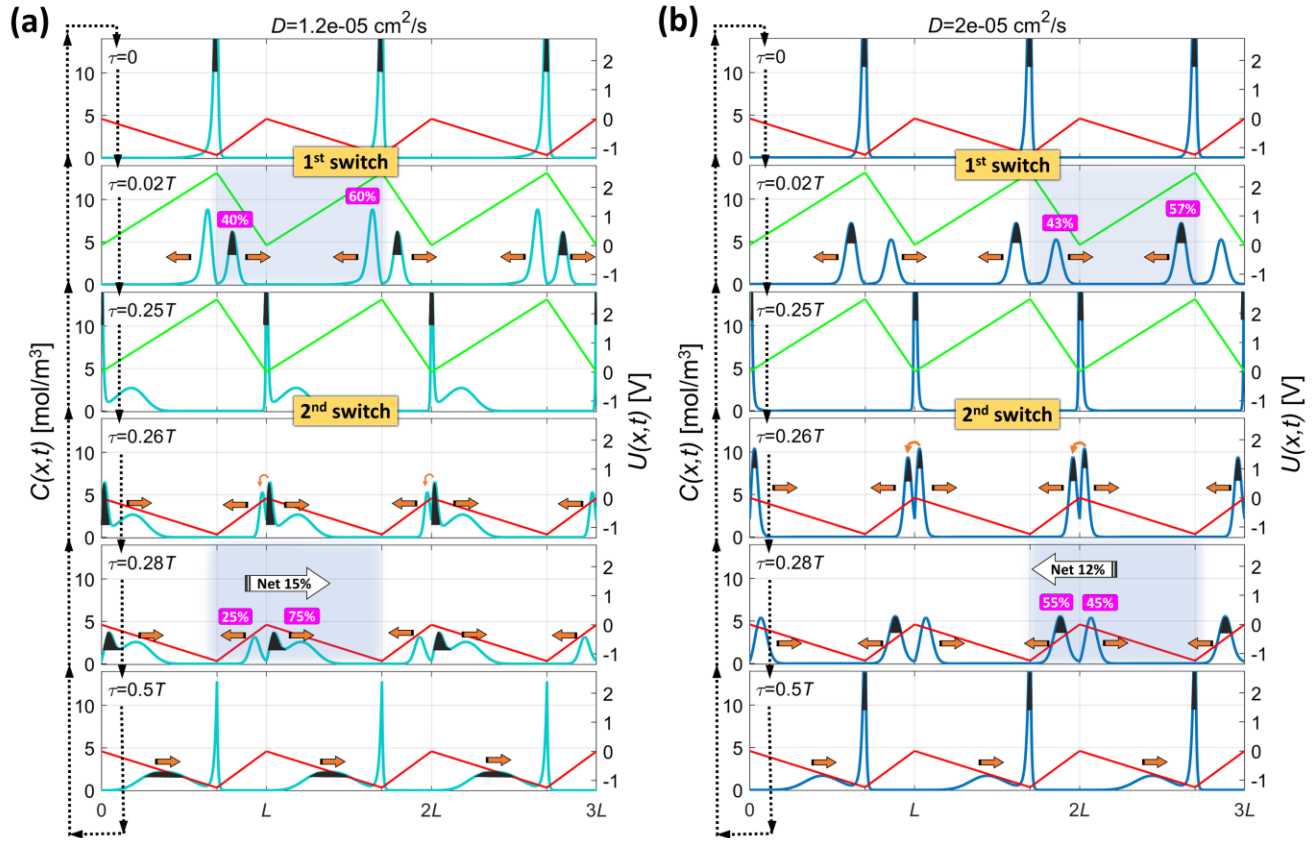

Fig. 3. The concentration response $C(x,t)$ of two positively charged monovalent ions ($z = 1$) with diffusion coefficients $D = 1.2 \cdot 10^{-5}$ cm^2/s (a), and $D = 2 \cdot 10^{-5}$ cm^2/s (b). The potential distribution $U(x,t)$ is shown on the right axis. The signal frequency is $f = 83$ kHz, and all other ratchet parameters are the same as in Fig. 2.

fraction of the low D ions reach the potential minimum before the second potential switch. As a result, the injection from right to left ($\tau = 0.28T$) is less significant, and while 60% of the ions are traveling to the left after the first potential switch, 75% return after the second switch, yielding a positive net velocity of about $v_{net} \approx 15\% \cdot L/T = 1.25$ cm/s.

Fig. 4 shows a 2D map of the net velocity of monovalent cations as a function of diffusion coefficient and the input signal frequency. All other ratchet parameters are as in Fig. 2. It can be seen that the stopping frequency increases linearly with the diffusion coefficient. Thus, at a given frequency, ions with diffusion coefficients above a specific value have a positive velocity, and ions with diffusion coefficients below that value travel in the opposite direction. For example, at a frequency of 60 kHz, Li^+ ($D = 1.03 \cdot 10^{-5}$ cm^2/s) ions travel forwards at a velocity of +0.6 cm/s, but K^+ and Na^+ ($D = 1.96 \cdot 10^{-5}$ and $D = 1.33 \cdot 10^{-5}$ cm^2/s respectively) ions travel backwards with velocities

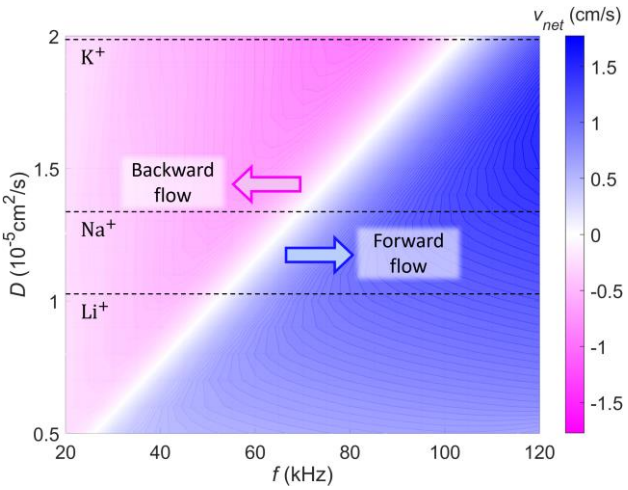

Fig. 4. Net velocity of monovalent cations as a function of their diffusion coefficient and the signal frequency. All ratchet parameters are the same as in Fig. 2.

of about –0.8 and –0.5 cm/s respectively. Moreover, since the input signal determines which ions move forward and which move backward, the ionic selectivity of these ratchets can be tuned in real time.

B. Normalized net ion velocity

To analyze the ratchet behavior for a wide range of parameters, the net ion velocity is normalized by a characteristic ion velocity parameter $v_0 = zD\beta V_{max}/L$. A normalized frequency, $\Gamma = f/f_0$, was also defined, where the characteristic frequency is $f_0 = v_0/L$. Once the normalized equations are solved, a single characteristic net velocity curve can be used to find the net velocity as a function of frequency for any diffusion coefficient or spatial period with appropriate reparameterization. Fig. 5(a) shows the normalized net ion velocity as a function of Γ (i.e., characteristic net velocity curves), for $\delta = 0.25$ and different symmetry factors, α. The net ion velocity is negative at low normalized frequencies for all values of α. However, at high normalized frequencies, the sign of the time-averaged potential, $\bar{U} = \delta V_{max} + (1-\delta)\alpha V_{max}$, determines the direction of the net velocity, and whether velocity reversal with frequency is possible. This can be seen in Fig. 5(a), where only curves that correspond with $\bar{U} < 0$ ($\delta = 0.25,\ \alpha < -0.33$) exhibit a normalized stopping frequency, Γ^* (crossing the $v_{net} = 0$ axis). The inset of Fig. 5(a) shows the same curves in a wider Γ range, illustrating a known ratchet property, that at very low and very high frequencies the output of a ratchet is zero [38]. A detailed analysis of the ratchet behavior as a function of normalized frequency and different symmetry factors is given in Appendix E. It is shown more generally that velocity reversal is possible only when the time averaged potential amplitude $\bar{U}$ has an opposite sign to V_{max}. Fig. 5(b) shows the normalized net ion velocity as a function of δ, for

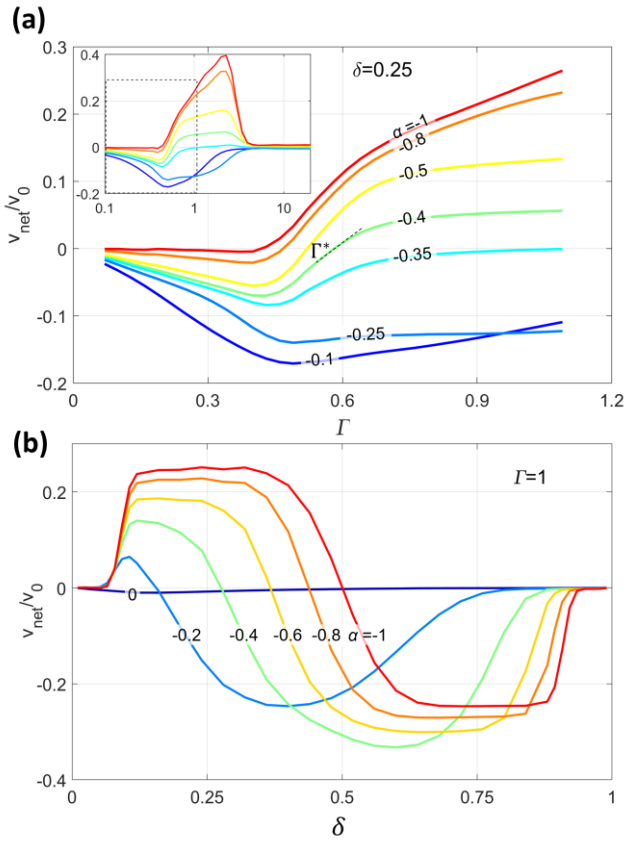

Fig. 5. Normalized net ion velocity, (a) as a function of normalized frequency, Γ (i.e., characteristic net velocity curves), for $\delta = 0.25$ and different symmetry factors, α. (b) As a function of duty cycle, δ, for $\Gamma = 1$ and different symmetry factors α. The ratchet parameters are: $x_c = 0.7$, $V_{max} = 2.5\,V$ (dimensional values used in calculation are: $L = 1\,\mu m$, $z = 1$, and $D = 1 \cdot 10^{-5}\,cm^2/s$).

$\Gamma = 1$, with different symmetry factors α. As expected, at $\delta = 0{,}1$ there is no net movement of ions since there are no temporal fluctuations. The net velocity is also zero at $\alpha = -1$, $\delta = 0.5$, since the potential distribution is temporally symmetric [38,48]. The behavior described by Fig. 5(b) is well known in ratchet systems [19,38,49], and is a good validation of our model.

C. Effect of concentration gradients

Velocity reversal was shown under the assumption of an infinitely periodic system in which no concentration gradient develops between spatial periods, and hence no work is performed. However, when driving ions between two finite reservoirs, an

initial concentration gradient can exist, or will develop during operation, which will impede further ion transport. Ion pumping will be maintained until the electrochemical potential difference building up due to the concentration gradient between the two reservoirs will match that supplied to the ions by the ratchet. Velocity reversal in the presence of an ion concentration gradient was demonstrated by simulating a finite ratchet domain, with several spatial periods, operating between two ion reservoirs with varying concentration ratios. The description of the model and the simulation results are given in Appendix F. It is shown that velocity reversal is possible even when the ions are transported up a concentration gradient with a concentration ratio as high as $C_1/C_2 = 10{,}000$ between two reservoirs. Such high concentration ratios are to be expected from a ratchet that is operated with a high potential input relative to the thermal voltage, $V_{max} \approx 40\frac{k_B T_r}{e}$ (@25℃), since the ions electrochemical potential difference between the reservoirs is proportional to $\frac{k_B T_r}{e}\ln(C_1/C_2)$. Furthermore, the maximal concentration gradient that the ratchet can overcome increases greatly with the number of the ratchet spatial periods. It should be noted that obtaining large concentration gradients between the two electrolyte reservoirs requires that no coulombic forces develop due to the separation of cations and anions. In the section V we discuss an interesting mode of operation in which both cations and anions are driven in the same direction by the ratchet. If both ions are transported in the same direction at the same velocity, local charge neutrality is maintained, and coulombic forces do not develop. A more detailed analysis of the ratchet drive against a concentration gradient, which also accounts for the coulombic interaction between ions is left for future work.

D. The separation resolution

The selectivity of membranes for different same-charge ions is typically expressed in terms of the ratio of fluxes of the desired and undesired species crossing the membrane [50,51]. A highly selective membrane will yield a flux ratio on the order of 100:1 for the wanted species, and typically much lower than that [51–55]. In the case where same-charge ions are transported in opposite directions, none of the unwanted ions will cross the membrane, and this selectivity definition ceases to be relevant. Thus, the *separation resolution*, $\mathcal{R}$, is introduced. It is defined as the ability to separate different same-charge ions according to the difference in their diffusion coefficients. By this definition, a ratchet membrane can separate two types of ions with a diffusion coefficient difference of ΔD, by driving one ion through the membrane at a velocity $v_{net} = \mathcal{R}\Delta D$, while the other ion is kept at its stopping frequency and is not affected by the ratchet. Since this definition describes a linear relation between the difference in diffusion coefficients and the ion net velocity, it becomes less accurate as ΔD increases.

The separation resolution for a certain set of ratchet parameters is calculated according to eq. (4) based on the normalized stopping frequency Γ^*, and the slope of the characteristic net velocity curve $v_{net}/v_0 = \mathcal{H}(\Gamma)$, as shown for example in Fig. 5(a) (the derivation of eq. (4) is given in Appendix A).

$$\mathcal{R}(\alpha, \delta, x_c, \beta V_{max}, L, z) = \left.\frac{\partial v_{net}}{\partial D}\right|_{\Gamma^*} = -\frac{z\beta V_{max}}{L}\Gamma^* \left.\frac{\partial \mathcal{H}}{\partial \Gamma}\right|_{\Gamma^*}. \quad (4)$$

Fig. 6(a) shows the separation resolution for different symmetry factors, α, and duty-cycles, δ. The light blue region corresponds to input signals that do not yield velocity reversal, showing again

that for $V_{max} > 0$, velocity reversal is possible only when $\bar{U} < 0$. High separation resolution is achieved using mid-range symmetry factors ($-0.8 < \alpha < -0.4$,) and mid-range duty-cycles ($0.2 < \delta < 0.4$). The effect of each variable cannot be examined separately because they are interconnected but can be generally understood by referring to eq. (4): (i) Low δ leads to lower Γ^*, since a larger time-period is needed to reach the steady state distribution at $\tau = t^+$. (ii) High α (in magnitude) reduces $\partial\mathcal{H}/\partial\Gamma|_{\Gamma^*}$, due to lower injection. (iii) A combination of high δ and low α (in magnitude) also reduces $\partial\mathcal{H}/\partial\Gamma|_{\Gamma^*}$, since it approaches $\bar{U} = 0$.

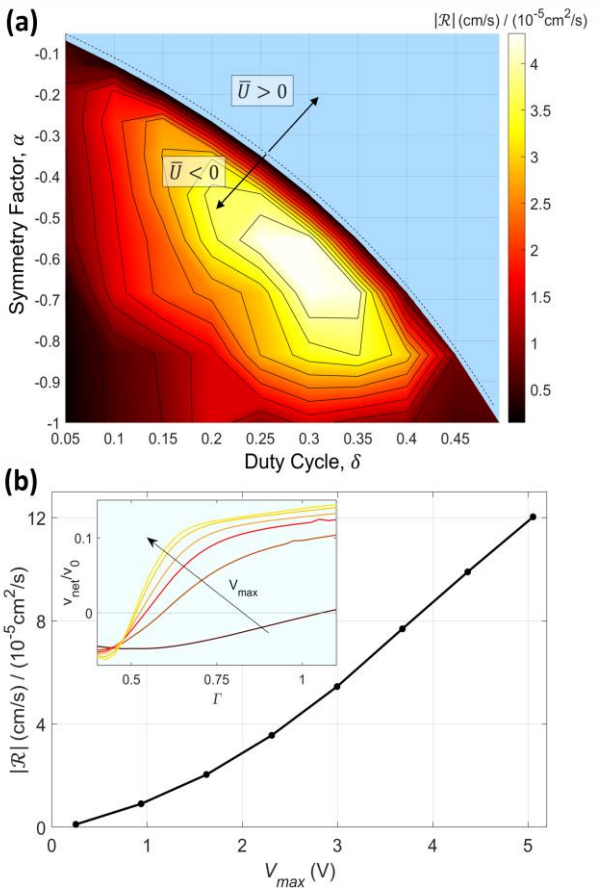

Fig. 6. (a) Separation resolution magnitude as a function of symmetry factor, α, and duty cycle, δ. (b) Separation resolution magnitude as a function of maximum amplitude V_{max}. The inset shows the characteristic net velocity curves. Unless stated otherwise in the figures, the ratchet parameters are: $\delta = 0.25, \quad \alpha = -0.5 \quad x_c = 0.7, \quad V_{max} = 2.5\,V$ (dimensional values used in calculation are: $L = 1\,\mu m$, $z = 1$, and $D = 1 \cdot 10^{-5}\ cm^2/s$).

The separation resolution is proportional to L^{-1}, therefore devices with a small spatial period are favorable since they will have a higher resolution. However, such devices will have to operate at much higher signal frequencies, since the stopping frequency is proportional to L^{-2}. The separation resolution also increases with V_{max}, as shown in Fig. 6(b). For lower potential amplitudes the increase is non-linear. This is due to the linear term of V_{max} in eq. (4) and an additional increase of the slope of the characteristic velocity curve, $\partial\mathcal{H}/\partial\Gamma|_{\Gamma^*}$, as shown in the inset. For higher values of V_{max} the separation resolution becomes linear with the amplitude reaching $\mathcal{R} = 12\ (\mathrm{cm/s})/(10^{-5}\mathrm{cm}^2/\mathrm{s})$ for $V_{max} = 5\,V$. Thus, for two monovalent ions with a difference in diffusion coefficients of $\Delta D = 0.01 \cdot 10^{-5}\ \mathrm{cm}^2/\mathrm{s}$, which is a relative difference of about 1% (for the prevalent ions in water), the maximum separation velocity is $\Delta v_{net} = \mathcal{R} \cdot \Delta D = 0.12\ \mathrm{cm/s}$. A detailed analysis of the effect of the spatial symmetry factor, x_c, and the ion valence, $|z|$, on the ratchet behavior and the separation resolution is given in Appendix G. We note that eq. (4) cannot be used to calculate the separating resolution of ions with different charge numbers, since different charge numbers result in different characteristic velocity curves (as shown in Fig. 12(c)). In addition, since drift currents are linear with the product of ions charge number and diffusion coefficient, the separation performance is determined by differences in the zD product. Therefore, a case-by-case method should be taken when studying ions with different charge numbers.

V. APPLICATIONS AND IMPLICATIONS

A. Extraction of trace ions from a solution

The unique ability of ratchets to drive particles with the same charge in opposite directions makes them very attractive for ion separation applications. This characteristic may be most significant when targeting the removal of trace ions from a solution where conventional membrane-based separation methods require extreme levels of selectivity. For example, Fig. 7(a) shows the net velocity as a function of frequency of lead (Pb^{2+}, $zD = 1.89 \cdot 10^{-5}\ cm^2/s$), copper ($Cu^{2+}$, $zD = 1.46 \cdot 10^{-5}\ cm^2/s$), lithium ($Li^+$, $zD = 1.03 \cdot 10^{-5}\ cm^2/s$), and sodium ($Na^+$, $zD = 1.33 \cdot 10^{-5}\ cm^2/s$). Lead can be extracted from contaminated drinking water, with a much higher sodium content, with a relatively high velocity since they have a high zD difference. However, copper which has a much closer zD value to sodium, cannot be separated from sodium with high velocities, since their stopping frequencies are very close. Lithium is conveniently positioned for extraction from sea water since it has one of the lowest zD values of cations. This means that even though its concentration in the ocean is very low (0.15 ppm) [56,57], it can be separated in a single process from most other cations that are present at much higher concentrations. The performance of a system for the extraction of lead ions out of drinking water is discussed in Appendix H.

B. Ambipolar ion transport for desalination

Velocity reversal can also be used for driving oppositely charged ions in the same direction, a process we term *ambipolar* ion transport. When both cations and anions are driven in the same direction, there is no charge separation, and therefore an opposing electrostatic potential does not develop, making this an attractive mechanism for desalination

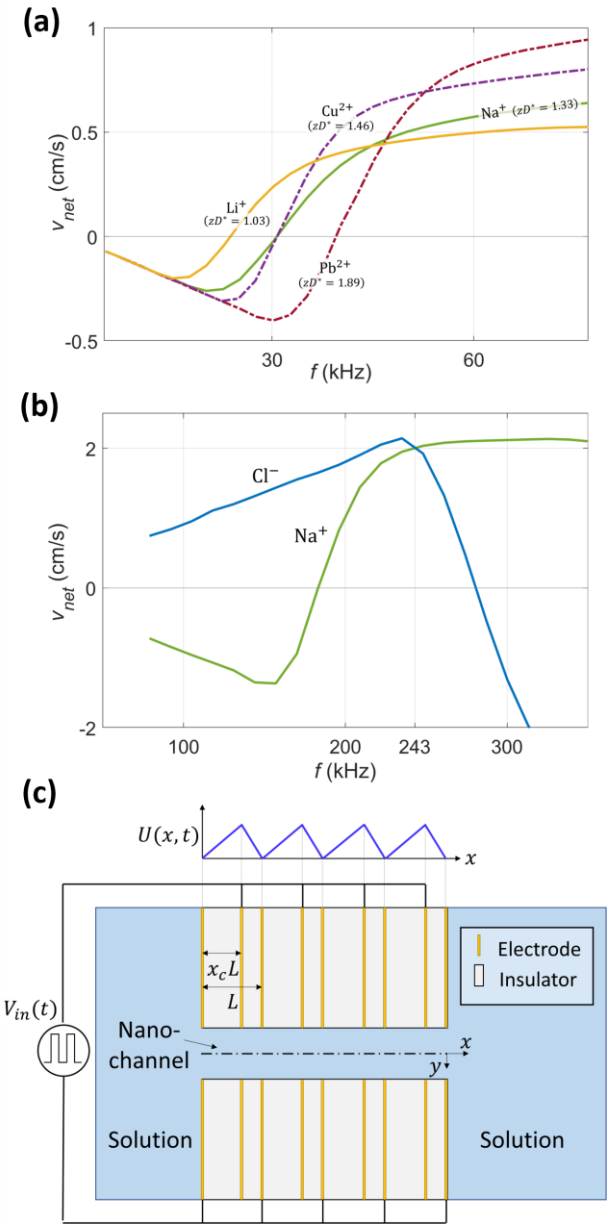

Fig. 7. (a) Net velocity of Na^+, Li^+, Cu^{2+}, and Pb^{2+} as a function of input signal frequency. The units for zD^* are in $(10^{-5} cm^2/s)$. Ratchet parameters: $L = 1\ \mu m$, $x_c = 0.7$, $V_{max} = 1\ V$, $\alpha = -0.5$, $\delta = 0.25$. (b) Net velocity of Cl^- and Na^+ showing ambipolar transport. Ratchet parameters: $L = 1\ \mu m$, $x_c = 0.6$, $V_{max} = 5\ V$, $\alpha = -0.38$, $\delta = 0.25$. (c) Conceptual scheme for a flashing ratchet with a saw-tooth electric potential in solution.

applications with a single membrane. Fig. 7(b) shows an example for ambipolar transport of the main ions in seawater. When the ratchet is operated at 243 kHz, both the negative and positive ions are

transported in the same direction at a velocity of 2 cm/s.

C. Device realization

Ions traveling within the ratchet device must experience relatively high driving electric potentials (with respect to the thermal voltage) for the ratchet to operate. However, in an electrolytic environment the potential imposed by the electrodes is screened due to double layer formation. Thus, the characteristic length scale of such devices must be in the order of the Debye length or smaller. Several works have realized devices that manipulate ion flow [58–60] using high potentials although none of them considered ratcheting. Our prior experimental demonstration of an RBIP device [37] has also shown that potential landscapes with high amplitudes can be implemented in solutions making ratchet driven ion pumping feasible.

Fig. 7(c) presents a conceptual scheme for a device that can realize a saw-tooth electric potential distribution in an electrolytic environment which can be modulated to generate a ratchet induced ionic current. Spatial asymmetry is achieved by alternating the spacing between each two electrodes along the x axis of the device. To avoid potential screening in moderate-to-high salinity solutions, the spatial length, L, and the nano-channel size should be in the order of 1-10 nm. However, it is reasonable to assume that much larger length scales, which are easier to obtain from a fabrication standpoint, would also result in potential distributions that are close to a saw-tooth shape, with similar ratcheting properties. The potential also decays in the transverse direction (y) away from the electrode, which reduces the ratchet performance at the center of the channel. Apart from the reduction in the induced ion velocity, this decay also affects the ratchet selectivity. An initial estimation of this effect can be found in Appendix I. High electric potentials in the nano-channel, with minimal faradaic reactions, can be obtained by coating the entire device (including the inner walls of the nano-channel) with a thin insulting layer, for example by Atomic Layer Deposition (ALD). A more detailed analysis of device geometry and structure is left for future work.

VI. CONCLUSIONS

In this work we have laid the theoretical groundwork for ratchet-driven ion separation. We have shown that a flashing ratchet can be used to drive ions with the same charge number in opposite directions based on the difference in diffusion coefficients. This unique ratchet property paves the way for rapid extraction of trace ions from solutions where conventional membrane-based separation processes do not offer sufficient selectivity. We define the ratchet separation resolution and show that under moderate voltages, ions with a 1% relative difference in diffusion coefficients can be driven in opposite directions with a velocity difference of 1.2 mm/s. Moreover, non-linearities in the ion velocity with the input signal amplitude and ion valence can be further utilized to enhance the separation resolution. Thus, ratchet-based ion pumping systems may prove beneficial for water treatment technologies, electrochemical CO_2 reduction, extraction of valuable metals from sea water, battery recycling and more.

ACKNOWLEDGMENTS

The authors would like to acknowledge Francesca Toma for helpful discussions. AH acknowledges the support of the Boris Mints Institute. JWA was supported by the Joint Center for Artificial Photosynthesis, a DOE Energy Innovation Hub, supported through the Office of Science of the United States. Department of Energy under Award No. DE-SC0004993. SA acknowledges the support

of the Gordon and Betty Moore Foundation under a Moore Inventor Fellowship (GBMF grant #5641) and The Beall Family Foundation (UCI Beall Innovation Award). GS thanks the Azrieli Foundation for financial support within the Azrieli Fellows program.

GS and SA conceptualized this work, AH and GS conducted the investigation, AH, JWA and GS designed the methodology, AH conducted the formal analysis and acquired the data, visualizations were designed by AH and GS, the original draft was written by AH and GS, and all authors contributed to its reviewing and editing. GS supervised the project, administered it, and acquired the funding for it.

Conflict of Interest

GS, JWA, and SA filed patent applications US 16/907,076 and US 17/125,341 for ratchet-based ion pumping membrane systems. There are no other conflicts of interest to declare.

APPENDIX A: METHODS

Continuity equation computational model

In the absence of bulk chemical reactions, the one-dimensional transport of noninteracting ions in a solution is determined by the continuity equation:

$$\frac{\partial C(x,t)}{\partial t} = -\frac{\partial}{\partial x} N(x,t), \qquad \text{(A1)}$$

where $C(x,t)$ is the ion concentration, and $N(x,t)$ is the ion flux. When convection is negligible, the ion flux is driven by drift and diffusion processes:

$$N(x,t) = -D\left[z\beta C(x,t)\frac{\partial}{\partial x}U(x,t) + \frac{\partial}{\partial x}C(x,t)\right]. \qquad \text{(A2)}$$

Here D is the ion diffusion coefficient, z is the ion charge number, $\beta = e/k_B T_r$ is the inverse thermal voltage, k_B is the Boltzmann constant, T_r is the temperature, and e is the elementary charge. Equations (1), (2), (A1), and (A2) were solved numerically using COMSOL® Multiphysics v5.5. The model domain is $x \in [0, L]$, with a periodic boundary condition defined as $C(0,t) = C(L,t)$, and a normalization condition was used for the total concentration $\int_0^L C(x,t)dx\,/L = c_0$, where c_0 is a reference ion concentration. The initial condition for the time-dependent simulation was the steady state concentration distribution calculated with the time-averaged potential distribution as an input: $\overline{U}(x) = [\delta + (1-\delta)\alpha]V(x)$. The time-dependent simulation was run over several consecutive temporal periods, until the net ion flux reached a steady state value, and the ratchet operation was independent of its initial condition. The convergence of the net ion flux was not limited by a strict condition, however, typically 4 temporal periods were enough to get a relative difference <1% between the average flux of the last two periods. The model predictions were validated by comparing them to prior analytical results under similar conditions, as described in Appendix C.

Detailed calculation of the separation resolution

We would like to find the separation resolution for any set of parameters, represented by a single characteristic net velocity curve $\mathcal{H}(\Gamma)$ and its corresponding normalized stopping frequency Γ^*. Applying the chain rule on the definition of the separation resolution, and remembering that at the normalized stopping frequency, $\mathcal{H}(\Gamma^*) = 0$, we obtain:

$$\mathcal{R} = \left.\frac{\partial v_{net}}{\partial D}\right|_{\Gamma^*} = \left.\frac{\partial\left(v_0\mathcal{H}(\Gamma)\right)}{\partial D}\right|_{\Gamma^*} = \frac{\partial v_0}{\partial D}\mathcal{H}(\Gamma^*) + v_0\left.\frac{\partial \mathcal{H}}{\partial D}\right|_{\Gamma^*} = v_0\left.\frac{\partial \mathcal{H}}{\partial \Gamma}\right|_{\Gamma^*}\left.\frac{\partial \Gamma}{\partial D}\right|_{\Gamma^*}, \quad \text{(A3)}$$

where:

$$\frac{\partial \Gamma}{\partial D} = \frac{\partial}{\partial D}\left(\frac{fL^2}{zD\beta V_{max}}\right) = -\frac{fL^2}{\beta V_{max} zD^2} = -\frac{\Gamma}{D}. \quad \text{(A4)}$$

Plugging (A4) into (A3) yields:

$$\mathcal{R} = \left(\frac{zD\beta V_{max}}{L}\right)\left(-\frac{\Gamma^*}{D}\right)\left.\frac{\partial \mathcal{H}}{\partial \Gamma}\right|_{\Gamma^*} = -\frac{z\beta V_{max}}{L}\Gamma^*\left.\frac{\partial \mathcal{H}}{\partial \Gamma}\right|_{\Gamma^*}. \quad \text{(A5)}$$

Numerical model for the diffusion equation

Assuming no convection and no electric field outside the electric double layer near the surface of the RBIP, the one-dimensional continuity equation is reduced to the transient diffusion equation:

$$\frac{\partial C(x,t)}{\partial t} = \mathrm{D}\frac{\partial^2 C(x,t)}{\partial^2 x}. \quad \text{(A6)}$$

Eq. (A6) was solved numerically within the domain $x \in [0, W/2]$, with the following initial and boundary conditions:

$$C(x,0) = c_0, \quad \text{(A7)}$$

$$\frac{\partial C}{\partial x}(0,t) = 0, \quad \text{(A8)}$$

$$N_{ext} = -D\frac{\partial C}{\partial x}\left(\frac{W}{2},t\right) = C\left(\frac{W}{2},t\right)v_{ext}. \quad \text{(A9)}$$

Here, eq. (A7) sets a uniform initial concentration in the entire domain, eq. (A8) defines symmetry around $x = 0$, and eq. (A9) defines the ionic flux at the edges of the feed channel, assuming a net ion velocity v_{ext} induced by the RBIP. The numerical analysis was done using the Crank-Nicolson method [61].

APPENDIX B: THE OPERATING PRINCIPLES OF A FLSHING RATCHET

Fig. 8(a) shows a schematic illustration of the operating principles of a flashing ratchet driving positively charged particles. The empty circles represent the ions position at the beginning of every step, and the filled circles represent their position at the end of every step. The potential distribution through the device (V, solid blue line) is switched between two saw-tooth potential distributions, V^+ and V^-, where $V^- = \alpha V^+$, and the potential asymmetry factor α is negative. Initially the particles rest at the potential minima, for example at x_1. When the potential is switched to V^- at $t = t_0$, the particles drift in both directions. The time interval between t_0

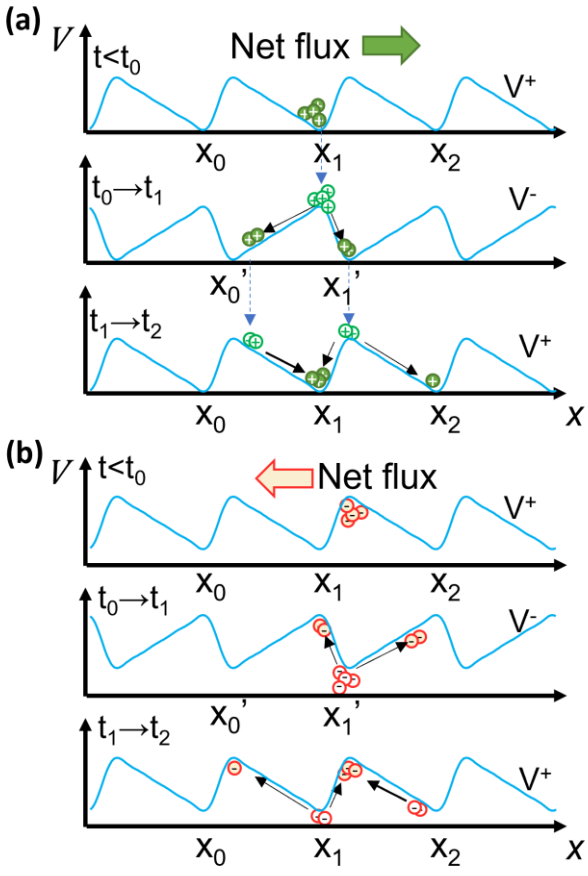

Fig. 8. An illustration of a flashing ratchet driving positively charged (a), and negatively charged (b) particles. The solid blue line illustrates the potential distribution during sequential steps, empty circles mark the position of particles at the beginning of every step and filled circles mark their position at the end of every step.

and t_1 is tuned to allow some drifting particles to reach the potential minimum on their right, x_1', but not the potential minimum to their left, x_0'. Hence, when the potential is switched to V^+ at $t = t_1$, some of the particles at x_1' drift further to the right towards x_2, but all the other particles return to their initial position at x_1 resulting in a net current to the right. The asymmetric potential distribution allows some particles to reach the potential minima in one direction before particles drifting in the opposite direction, thus making it essential for a non-zero net current. Fig. 8(b) illustrates the operation of the same ratchet driving negatively charged particles. Here particles drift towards the potential peaks and as a result, the same potential distribution and input signal generate a net particle flux in the opposite direction.

APPENDIX C: MODEL VALIDATION

To validate our numerical model, we compare our simulation to the analytical solution presented by Kedem et al. [19], and developed by Rozenbaum et al. [49] for low energy flashing ratchets (compared to the thermal energy). The analytical solution uses a biharmonic potential distribution, given in eq. (C1):

$$V(x) = V_1 \sin(2\pi x/L) + V_2 \sin(4\pi x/L). \quad \text{(C1)}$$

The amplitudes are defined as $V_1 = V_{max}$ and $V_2 = V_{max}/5$ to get a spatially asymmetric potential that is similar in shape to a sawtooth. The particles net velocity is calculated by eq. (C2):

$$v_{net,analytic} = \frac{\pi}{4}\frac{D}{L}\beta^3 V_1^2 V_2 (1-\alpha)^2 [(1+\alpha)\Phi_1(\Gamma,\delta) + (1-\alpha)\Phi_2(\Gamma,\delta)],$$

$$\Phi_1(\Gamma,\delta) = \frac{12}{\pi^2} xC(x,y), \;\; \Phi_2(\Gamma,\delta) = \frac{12}{\pi^2} xG(x,y),$$

$$x = \beta V_{max}\Gamma/(2\pi), \;\; y = 2\pi(1-\delta),$$

$$C(x,y) = \sum_{n=1}^{\infty} \frac{x(7+2x^2n^2)(1-\cos yn)}{(1+x^2n^2)^2(16+x^2n^2)}, \quad G(x,y) = \left(1 - 2\frac{y}{2\pi}\right) C(x,y) - \frac{D(x,y)}{2\pi}, \quad \text{(C2)}$$

$$D(x,y) = \sum_{n=2}^{\infty} \sum_{m=1-n}^{-1} [B(x,y,n,m) + B(x,y,m,n)] + \sum_{n,m=1}^{\infty} B(x,y,n,m),$$

$$B(x,y,n,m) = \frac{x[5n + (n+m)(4-x^2n^2)][\sin yn\,(1-\cos ym) + \sin ym\,(1-\cos yn)]}{(n+m)m(1+x^2n^2)(16+x^2n^2)(1+x^2(n+m)^2)}.$$

To compare our numerical model to the analytical model, simulations are performed with the potential distribution defined by eq. (C1). Fig. 9 shows a comparison of the normalized net velocity as a function of the normalized frequency, calculated with both models, for different potential amplitudes. The two models agree well for low amplitudes, i.e., $\beta V_{max} < 1$ ($V_{max} < 25.7$ mV, @25℃), while for higher amplitudes the models diverge and the analytical solution over-estimates the ratchet performance. This result is to be expected since the analytical model was developed assuming low energy inputs. Since ion transport problems usually require higher potentials to drive a sufficient current, this emphasizes the need for a numerical solution.

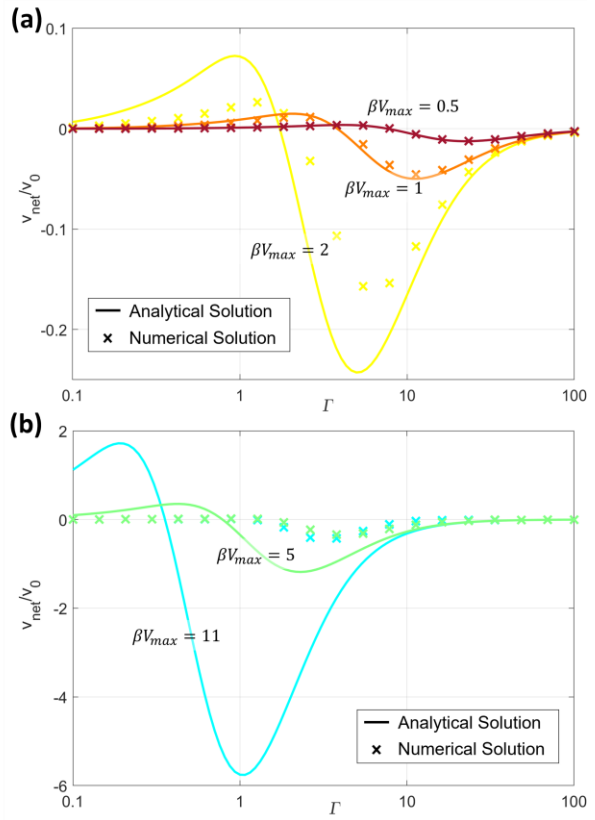

Fig. 9. Numerical vs. analytical solution for a potential distribution described by eq. (C1). Ratchet parameters: $L = 10\ \mu m$, $\alpha = -0.75$, $\delta = 0.25$, and βV_{max} between (a) 0.5 to 2, and (b) 5 to 11 (b).

APPENDIX D: INSTANTANEOUS VELOCITY ANALYSIS

The instantaneous average ion velocity, $\bar{v}(\tau)$, is defined as the spatial average ion flux, $\bar{N}(\tau) = \int_0^L \frac{N(x,\tau)}{L}\, dx$, divided by the reference concertation, c_0. Fig. 10(a) shows the variation of the instantaneous average velocity over a single time-period for the low *D* and high *D* ions, which are presented in Fig. 2 and Fig. 3, with the same ratchet parameters, and at a signal frequency $f = 83$ kHz. The inset shows the integral of $\bar{v}(\tau)$ up to a point τ, divided by the time-period *T*. This value represents the contribution to the net velocity up to a time point τ.

Fig. 10(b-g) shows the ions concentration and potential distribution at selected time points. Collectively, these figures allow to analyze and assess the contribution of different parts of the time-period to the net velocity. Closely after the beginning of the cycle, there is a short period in which different groups of ions are traveling in opposite directions, as shown in (c), resulting in an overall positive flux, due to the higher flux of the groups that are travelling in the high field section of the sawtooth. At point (d), there is only movement in the negative direction in the low field section, resulting in a negative flux. Overall, up to the potential switch at $\tau = 0.25T$ (point (e)), the total contribution to the net velocity is negative for both ions, but for the high *D* ion it is more negative, as can be seen in the inset of Fig. 10(a), mainly due to their higher mobility. After the potential switch, there is again a short period in which different groups of ions are traveling in opposite directions, as shown in (f). For the high *D* ion, this is accompanied by considerable injection of ions from the low to high field section of the sawtooth (see discussion on the injection phenomenon in section IV), leading to a dip in $\bar{v}(\tau)$, and an additional contribution to the net negative velocity, as shown in the inset. At the same time, most of the high *D* ion population is traveling in the positive direction under the influence of the low field, and although there is another group traveling in the opposite direction, this group is much smaller, so the overall flux is positive. The final period, represented by point (g), shows both ions traveling in the positive direction in the low field section. Interestingly, the instantaneous average velocity for both ions is equal, although they have different diffusion coefficients, due to the larger population of the low *D* ions.

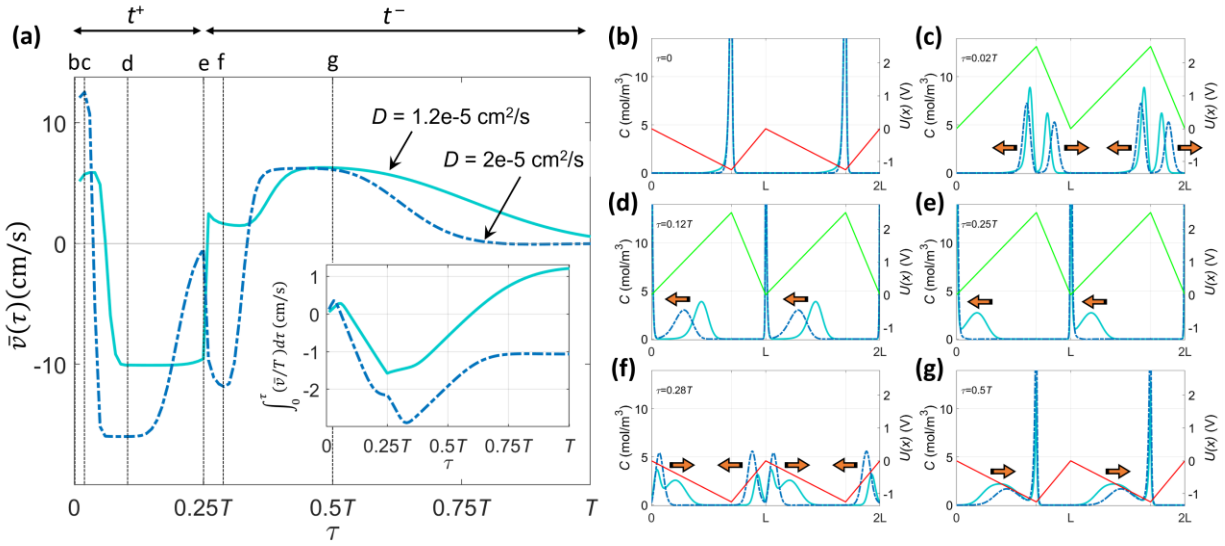

Fig. 10. (a) Instantaneous average ion velocity, $\bar{v}(\tau)$, along a time-period. The inset shows the integral of $\bar{v}(\tau)$ up to a point τ, divided by the time-period T. (b)-(g) Ion concentration (left axis) and ratchet potential (right axis) at various points along the time-period, marked in (a). All graphs show curves for two monovalent ions ($z = 1$) with diffusion coefficients $D = 1.2 \cdot 10^{-5}$ cm^2/s , and $D = 2 \cdot 10^{-5}$ cm^2/s. The ratchet parameters are: $L = 1$ μm, $x_c = 0.7$, $V_{max} = 2.5$ V, $\delta = 0.25$, $\alpha = -0.5$, and signal frequency is $f = 83$ kHz.

As a result of this, and of the fact that the high D ions reach the potential minimum at about $\tau = 0.75T$, the contribution of this final period to the net velocity is more positive for the high D ion. Taken together, these results show the contribution of each part in the time-period and explain why the overall net velocity of the low D ion is positive, and of the high D ion negative. Note that the value of the curves in the inset of Fig. 10(a), at $\tau = T$, is exactly the net velocity, as defined by eq. (3).

APPENDIX E: RATCHET BEHAVIOR AS A FUNCTION OF NORMALIZED FREQUENCY AND SYMMETRY FACTOR

Fig. 5(a) shows the normalized net ion velocity, as a function of Γ, for $\delta = 0.25$ and different symmetry factors, α. For moderately low normalized frequencies ($\Gamma < 0.45$ for this case where $\delta = 0.25$) the mechanism that determines the net velocity is similar to the one shown in Fig. 3(b), where the negative net velocity is a result of the injection phenomenon as described in section IV. As α decreases in magnitude, the injection becomes more dominant, and therefore the net velocity becomes more negative. For moderately high normalized frequencies ($\Gamma > 1$), the driving mechanism is similar to the one illustrated in Fig. *8*. The input signal frequency is low enough to allow ions to cross the high field section of the sawtooth potential before the potential switch, but high enough such that they cannot cross the low field section. An example for this kind of behavior is demonstrated in Fig. 3(a). In this frequency range the sign and magnitude of the net velocity are determined by the value of the time-averaged potential, $\bar{U} = \delta V_{max} + (1 - \delta)\alpha V_{max}$. For $\bar{U} < 0$ the ions are on average closer to the sawtooth tip ($x = x_c L$), and therefore most ions do not reach the sawtooth bases ($x = 0, L$) at any point in time. As a result, there is no significant injection, and the net velocity is positive, as demonstrated in Fig. 3(a). When $\bar{U} > 0$ the ions are on average closer to the sawtooth bases ($x = 0, L$), and as a result there is

significant injection, leading ions to diffuse over the barrier at x_c, resulting in a negative net velocity. Considering the entire frequency range, this shows that a velocity reversal for $V_{max} > 0$ is possible only when $\bar{U} < 0$, or more generally, when the time averaged potential $\bar{U}$ has sign opposite to V_{max}. This conclusion is also true for negatively charged ions or for potential distributions with an opposite spatial symmetry, i.e. $x_c < 0.5$. The only difference is that the characteristic velocity curves will be flipped with respect to $v_{net} = 0$, as demonstrated in Fig. 7(b) and Fig. 12(a).

APPENDIX F: VELOCITY REVERSAL IN THE PRESENCE OF CONCENTRATION GRADIENTS

To analyze the ratchet operation in the presence of a concentration gradient, ratchets with either 3 or 5 spatial periods were modeled. A diagram of the model is shown in Fig. 11(a). The concentration at the external boundaries is fixed, to simulate two infinitely large ion reservoirs beyond the simulation domain, with C_L and C_R being the ion concentration on the left and right boundaries, respectively. The ratchet region is defined by a periodic sawtooth potential, as expressed in eq. (1)-(2), and a period length $L = 1\,\mu\text{m}$. Between the ratchet and the boundaries are two regions, each with a width of $1.5L$, where the potential is set to 0. These regions are termed the *diffusion regions*. The concentration ratio C_L/C_R is defined, such that the ion concentration on the side with the lower concentration is set to $1\,\text{mol/m}^3$. The initial concentration in the diffusion regions is set to be equal to the concentration at the adjacent boundaries and is linear along the ratchet itself. The transient continuity equation (eq. (A1)-(A2)) is solved numerically using COMSOL® Multiphysics v5.5. The time-dependent simulation is solved over many temporal periods, until the per period net ion flux at the boundaries converges to a steady state value, and the ratchet operation is independent of its initial condition. The ratchet parameters are: $x_c = 0.7$, $V_{max} = 1\,\text{V}$, $\delta = 0.25$, $\alpha = -0.5$, and $f = 20, 40\,\text{kHz}$. The ion properties are: $z = 1$, $D = 1 \cdot 10^{-5}\,\text{cm}^2/\text{s}$.

Fig. 11(b) and Fig. 11(c) show the steady state ion flux due to the ratchet operation, as a function of the concentration ratio for $f = 20\,\text{kHz}$ and $f = 40\,\text{kHz}$, respectively. The solid lines are for the two ratchet models described above, with 3 and 5 spatial periods. The 'Ratchet off' flux is presented for reference (dashed lines). This flux is calculated for the same model domain and boundary conditions, but with zero potential applied in the entire simulation domain. Therefore, it represents the steady state diffusion flux that would arise between the two reservoirs, in the case that a ratchet potential is not applied. For example, for the 5 periods ratchet the 'Ratchet off' flux is $D(C_L - C_R)/(1.5L + 5L + 1.5L)$. At $f = 20\,\text{kHz}$, which is equivalent to a normalized frequency of $\Gamma = 0.5$, the ratchet drives a negative flux at $C_L/C_R = 1$. This result is in line with the findings for an infinitely periodic model, as presented in section IV, that predicts a negative velocity for the same normalized frequency and ratchet parameters (see Fig. 5(a)). The ratchet is driving ions in the same direction as the flux due to the concentration gradient when the concentration is higher in the right reservoir ($C_L/C_R < 1$). Hence, there is an increase in the flux magnitude compared to the 'Ratchet off' flux, as can be seen in the inset. On the other hand, when $C_L/C_R > 1$ the ratchet operation is opposed by the concentration gradient.

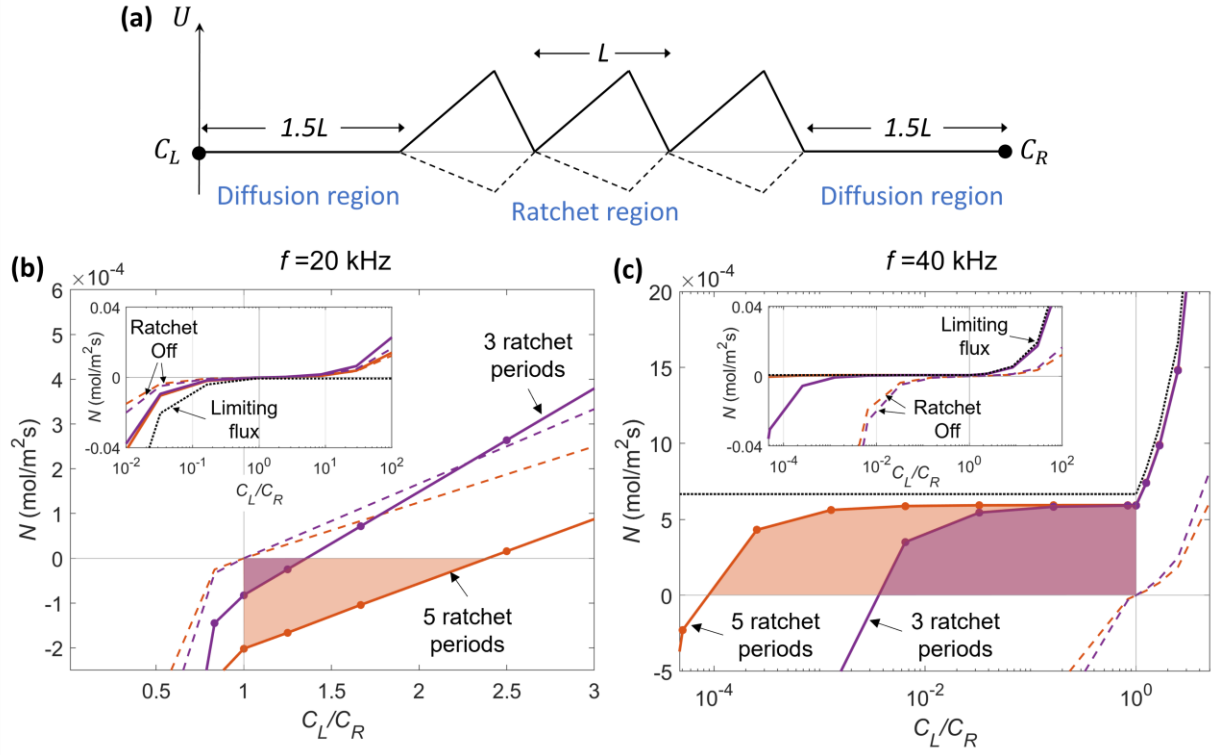

Fig. 11. (a) Model diagram showing the potential distribution for three spatial periods ratchet, and the concentration boundary conditions definition. (b-c) Ion flux, N, as a function of the concentration ratio between the left and right reservoirs, C_L/C_R, with ratchet signal frequencies $f = 20\ kHz$ (b), and $f = 40\ kHz$ (c). The insets show the same data set on wider flux and concentration ratio ranges. Ratchet parameters are: $L = 1\ \mu m$, $x_c = 0.7$, $V_{max} = 1\ V$, $\delta = 0.25$, and $\alpha = -0.5$. The ion properties are: $z = 1$, $D = 1 \cdot 10^{-5}$ cm^2/s. The ion concentration on the side with the lower concentration is set to 1 mol/m^3.

At low concentration ratios the flux is negative, but as the opposing concentration increase, diffusion becomes dominant, and the direction of the flux is reversed. It can be seen in Fig. 11(b) that the 5 periods ratchet can overcome a ratio up to $C_L/C_R = 2.3$, while the 3 periods ratchet can only overcome a modest ratio of $C_L/C_R = 1.3$. Surprisingly, as the concentration ratio increases further, the flux becomes higher than the 'Ratchet off' flux, especially with the 3 periods ratchet. The reason is that the ratchet, which is unable to oppose the larger concentration on the left, causes a local accumulation of ions in the right diffusion region. This accumulation increases the concentration gradient in the right diffusion region, and therefore the flux to the right, compared to the 'Ratchet off' flux. At $f = 40$ kHz, which is equivalent to a normalized frequency of $\Gamma = 1$, the ratchet drives a positive flux at $C_L/C_R = 1$. Here too, this result is in line with the infinitely periodic model that anticipates a positive velocity for the same ratchet parameters and $\Gamma = 1$ (see Fig. 5(a)). When the concentration is higher in the left reservoir ($C_L/C_R > 1$), the gradient and ratchet are acting in the same direction, hence there is an increase in flux magnitude relative to the 'Ratchet off' flux. When the ratchet operation is opposed by the concentration gradient ($C_L/C_R < 1$), it overcomes a significantly larger gradient compared to the same ratchet, driven at a frequency of $f = 20$ kHz. As can be seen in Fig. 11(c), the 3 periods ratchet can pump ions up to a ratio of about $C_R/C_L = 300$, while the 5 periods ratchet can reach a ratio of about $C_R/C_L = 10000$.

The maximal flux that can be induced by the ratchet in this model is limited by diffusion in the diffusion regions. For example, if the ratchet drive is to the positive direction, as is the case when $f = 40$ kHz, the maximal flux is achieved when the concentration at the left edge of the ratchet region is zero, and the limiting flux is $DC_L/1.5L$. This limiting flux (dotted line) is presented in Fig. 11(b-c). It can be seen that the ratchet induced flux matches the limiting flux, and only starts to decrease in magnitude at about $C_R/C_L = 10$, and $C_R/C_L = 200$, for the 3 and 5 periods ratchet, respectively. Thus, this is the opposing concentration ratio, at which the ratchet is no longer the most dominant driving force. It is noted that the limiting flux is constant for $C_L/C_R < 1$, since C_L is defined as constant in this range. At $f = 20$ kHz the limiting flux is never reached, indicating that the flux is limited by the ratchet performance and not by the diffusion regions.

Together these results provide important insights for the design of ion pumping systems. To drive ions against a large concentration gradient, one should design a system with as many ratchet spatial periods as possible, and work at a moderately high signal frequency, such as the case shown in Fig. 11(c).

APPENDIX G: THE EFFECT OF SPATIAL ASYMMETRY FACTOR AND ION VALENCE ON THE RATCHET BEHAVIOR AND THE SEPARATION RESOLUTION

Fig. 12(a) and Fig. 12(b) shows the effect of x_c on the net velocity characteristic curves, and the separation resolution, respectively. As might be expected, when the potential distribution is spatially symmetric, at $x_c = 0.5$, there is no net ion movement, and the separation resolution is zero. Interestingly, the optimal sawtooth shape for separation is with a moderate asymmetry, $x_c = 0.4$ & 0.6, and as x_c moves towards 0 or 1, the magnitude of $\mathcal{R}$ decrease. A key factor in this behavior has to do with the increase in length of the low field section. Injection requires that ions cross the entire low field section; thus, a longer path for ions to cross implies that injection will occur at a lower normalized frequency. This is apparent in Fig. 12(a), where the normalized stopping frequency decrease as the sawtooth becomes more spatially asymmetric, which according to eq. (4), leads to a decrease in the separation resolution.

Fig. 12(c), shows the characteristic velocity curves for different ion valence $|z|$. The inset shows the values of the separation resolution (between same-charge ions) as a function of ion valance. The separation resolution increases significantly with $|z|$, due to the linear term in eq. (4), and an increase of the slope $\partial\mathcal{H}/\partial\Gamma|_{\Gamma^*}$.

Fig. 12(a) also shows that ratchets with moderate spatial asymmetry, such as $x_c = 0.6$, exhibit a 'resonance like' behavior. For $x_c = 0.6$, most normalized frequencies result in a low velocity, but there is a relatively narrow Γ range that produces high positive velocities. The resonance like behavior is due a net velocity rise at a higher normalized frequency, $\Gamma = 0.6$, and a net velocity drop at a lower normalized frequency, $\Gamma = 3$ (compared to a velocity rise at $\Gamma = 0.5$ and drop at $\Gamma = 5$ for $x_c = 0.7$). The reason for the late rise in net velocity is described in section IV when discussing the separation resolution; and has to do with the frequency at which ions do not have enough time to cross the low field section of the sawtooth potential. The net velocity drop occurs when the ions do not have enough time to cross the

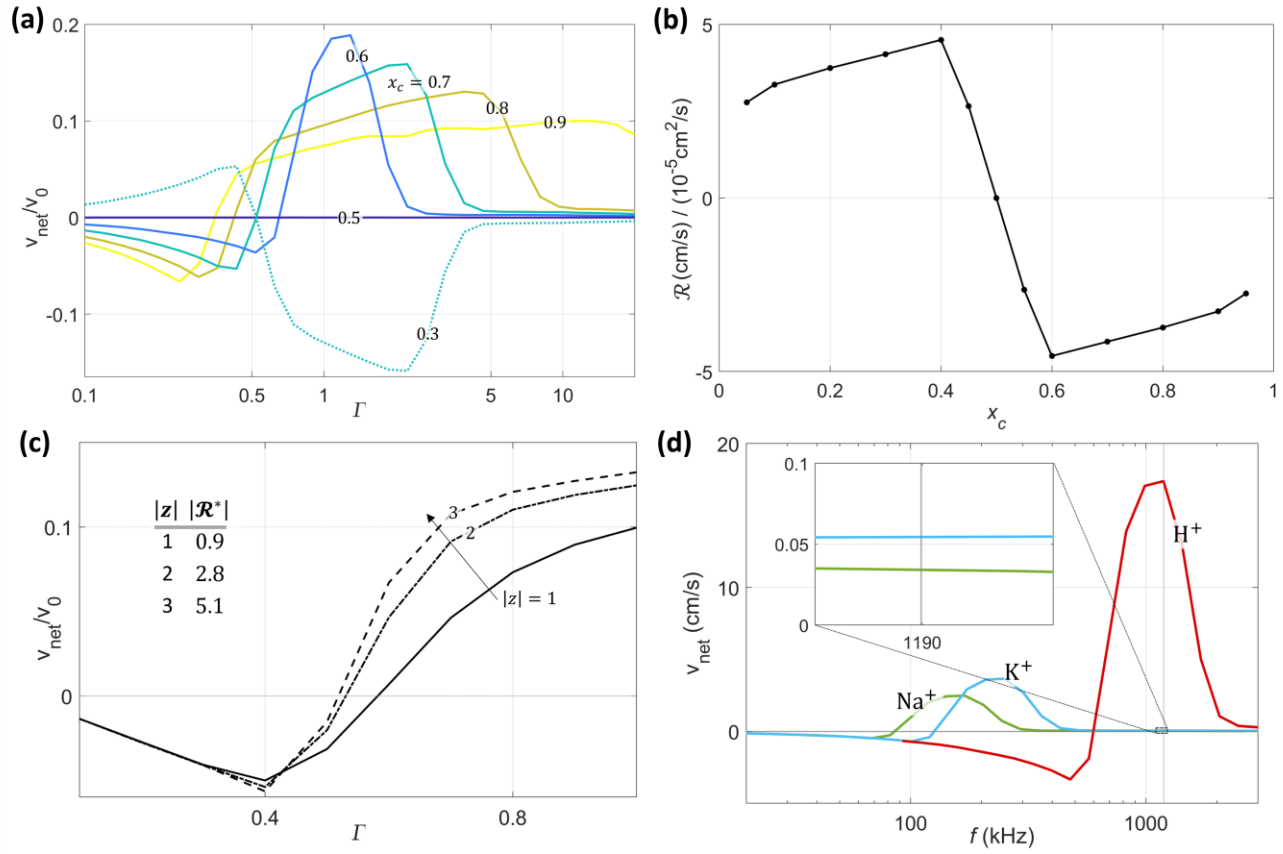

Fig. 12. (a) Characteristic net ion velocity curves for different x_c. (b) Separation resolution as a function of x_c. (c) Characteristic net velocity curves for different ion valence $|z|$, with $V_{max} = 1\,V$. The inset table shows the separation resolution between same-charge ions. $|\mathcal{R}^*|$ is in units of $(cm/s)/\,(10^{-5}cm^2/s)$. In (a-c), unless stated otherwise the ratchet parameters are: $x_c = 0.7$, $V_{max} = 2.5\,V$ (dimensional values used in calculation are: $L = 1$ μm, $z = 1$, and $D = 1 \cdot 10^{-5}$ cm^2/s). (d) Net velocity of Na^+, K^+, and H^+ as a function of input signal frequency. The net velocity curves were calculated from the normalized characteristic curve presented in (a) for $x_c = 0.6$, using the appropriate diffusion coefficient ratio for each ion. Na^+: $D = 1.33 \cdot 10^{-5}\ cm^2/s$, K^+: $D = 1.96 \cdot 10^{-5}\ cm^2/s$, H^+: $D = 9.31 \cdot 10^{-5}\ cm^2/s$.

high field section of the sawtooth. Since at $x_c = 0.6$ the high field section of the sawtooth potential is longer, this happens at relatively low normalized frequency, $\Gamma = 3$. The 'resonance like' phenomenon can be used when there is a need for high selectivity (not separation), and the diffusion coefficients are not very close. For example, in microbial fuel cells (MFCs) systems [62], there is a great need to achieve high selectivity for H^+ with respect to Na^+ and K^+. Fig. 12(d) shows the net velocity curve of the three ions as a function of the signal frequency. Since H^+ have a much higher diffusion coefficient, when the ratchet is operated at $f = 1200$ kHz, H^+ is at the middle of its 'resonance' range, but for Na^+ and K^+ this is experienced as a very high frequency, and their net velocities are approaching zero. The result is a net velocity ratio of 520:1 and 320:1 for H^+ with respect to Na^+ and K^+, respectively.

APPENDIX H: SELECTIVE ION EXTRACTION SYSTEM

To estimate the performance of a selective ion extraction system, a one-dimensional system was considered, as shown in the inset of Fig. 13. The system consists of a feed compartment with a width W=1 mm, and two RBIP membranes on its edges (x=±W/2) that extract the ion of interest out of the feed compartment with a constant net ion velocity, termed the extraction velocity. Assuming no convection in the feed compartment, and no electric field outside the electric double layer near the surface of the RBIP, the ion concentration was found by numerically solving the transient diffusion equation with a flux boundary condition at the edges, as described in Appendix A. The main graph in Fig. 13 shows the time required to extract lead ions out of the feed compartment as a function of the extraction velocity. The initial lead ion concentration is 100 ppb, and the extraction time is the time required to extract 99% of lead ions. The inset shows the time evolution of the lead ion distribution in the feed compartment. The extraction velocity is 0.01 cm/s, which is roughly the velocity at which the extraction time saturates. Soon after the extraction begins, the concentration at the edges approaches zero, and further extraction is limited by diffusion from the bulk solution. Thus, such systems can be optimal for applications where only a moderate portion of the ions should be removed rapidly. Nevertheless, for systems that are limited by diffusion in the bulk solution, the ratchet induced ion velocity can be as low as 0.01 cm/s without impeding the system performance. The ion extraction time can be decreased substantially by introducing stirring or by reducing the width of the feed compartment to micrometer scale. In such cases ion transport will no longer be limited by bulk diffusion and higher extraction velocities can be utilized.

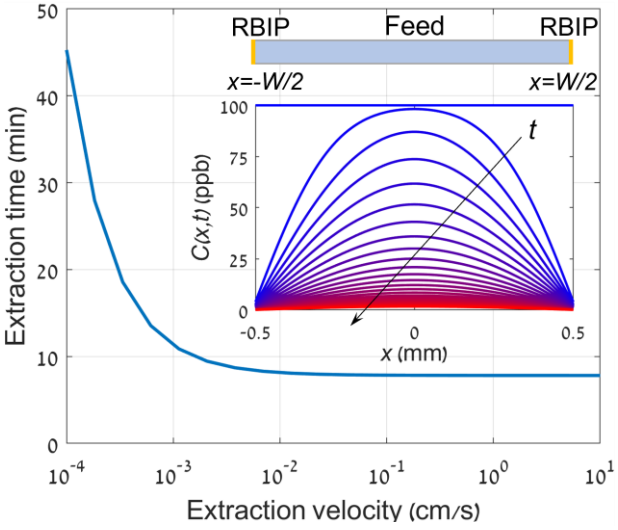

Fig. 13. Time to extract 99% of lead ions out of the feed compartment as a function of the extraction velocity. The inset shows the one-dimensional system model, and the time evolution of the lead ion distribution in the feed compartment, using an extraction velocity of 0.01 cm/s. Time step between two adjacent curves is 20 sec.

APPENDIX I: EFFECT OF ELECTRIC POTENTIAL DECAY ON THE ION SEPARATION PROPERTIES

The ratchet's ability to separate same-charged ions in opposite directions is based on the difference in the stopping frequencies of different ions. As shown in Fig. 7(b), the stopping frequency decreases as the electric potential amplitude decreases, which occurs at locations farther from a charged surface. This potential distribution can be found by solving the Poisson–Boltzmann equation and obtaining a characteristic Debye screening length that describes the distance in which the potential decays into the solution. Therefore, different locations along the transverse direction of the device will experience different potential amplitudes. As a result, different regions will have different frequency responses, which might reduce the overall separation resolution

of the device. To illustrate this, we consider the extraction of lithium (Fig. 14(a)) and lead (Fig. 14(b)) from a high sodium concentration solution. The solid curves represent the ion response very close to the surface of the electrode, where a potential $V_{max} = 1\,\mathrm{V}$ is applied. The dashed and dotted curves represent locations farther away from the surface, where the potential amplitude decays to $0.85\,\mathrm{V}$ and $0.8\,\mathrm{V}$, respectively. In an ideal device without potential decay, and thus an infinite Debye screening length, lithium can be extracted with a ratchet frequency slightly below the stopping frequency of sodium (30.8 kHz), where sodium has a very small negative velocity, and lithium is extracted with a large positive velocity. However, at this frequency even a small potential decay results in both ions having positive velocities, counteracting the separation process. Hence, to separate ions everywhere within the device, the ratchet should be operated at a frequency that supports ion separation over the entire range of potential amplitudes across the transverse direction of the device.

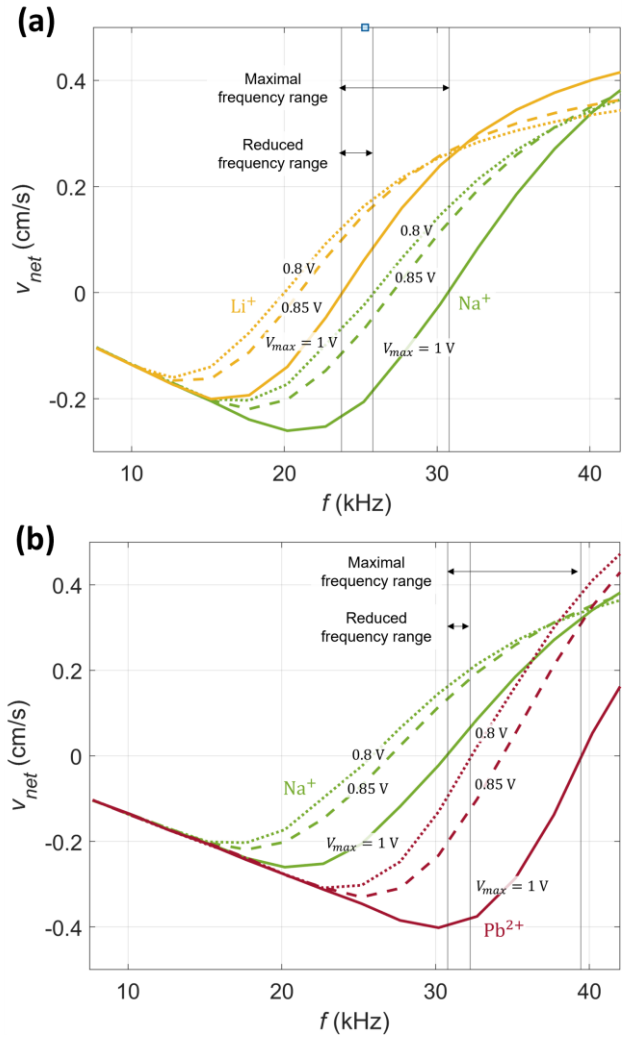

Fig. 14. Net ion velocity as a function of input signal frequency for the extraction of Li^+ from Na^+ (a), and Pb^{2+} from Na^+ (b). Solid, dashed, and dotted lines are for $V_{max} = 1\,V$, $0.85\,V$, and $0.8\,V$, respectively. The ratchet parameters: $L = 1\,\mu m$, $x_c = 0.7$, $\alpha = -0.5$, $\delta = 0.25$.

For example, lithium can be extracted by a device in which the potential amplitude decays from 1 V to 0.8 V or slightly lower (Fig. 14(a)). If the potential reduction in the transverse direction is not considered, ions are driven in opposite directions for every frequency between the stopping frequency of lead at an amplitude of 1 V, and the stopping frequency of sodium at the same amplitude. This frequency range is denoted maximal frequency range in Fig. 14(a-b). However, when considering the potential decay in the transverse direction, the amplitude of the input signal varies within the device. Thus, in order to drive the ions in opposite directions everywhere in the device, the input signal frequency should be lower than the lowest stopping frequency of sodium, at 0.8 V, and higher than the highest stopping frequency of lithium (and vice-versa when removing lead from sodium). This frequency range is denoted reduced frequency range in Fig. 14(a-b). In this frequency range, separation to opposite directions is possible, but the average device extraction velocity, and thereby the separation resolution, are lower. Similarly, when removing lead from sodium, potential decay results in a shift in the stopping frequency towards lower frequencies. However, in the case of lead, it is possible to operate the ratchet with the same frequency as in an ideal device, which is slightly above the stopping frequency of sodium (30.8 kHz). This is because lead has a higher stopping frequency

than sodium, so when the potential decays to 0.8 V or slightly lower (Fig. 14(b)), sodium maintains its positive velocity, while lead is still driven to the opposite direction. The average device extraction velocity is reduced compared to an ideal device, but to a lesser degree than the case of lithium, since most lead ions that are close to surface of the electrode are driven at their maximum velocity. Further investigation of these effects requires coupling the Poisson equation to the continuity equations in a multi-dimensional geometry which is beyond the scope of this work.

---

[1] C. Tang and M. L. Bruening, *Ion Separations with Membranes*, J. Polym. Sci. **58**, 2831 (2020).

[2] R. Epsztein, R. M. DuChanois, C. L. Ritt, A. Noy, and M. Elimelech, *Towards Single-Species Selectivity of Membranes with Subnanometre Pores*, Nat. Nanotechnol. **15**, 426 (2020).

[3] D. S. Sholl and R. P. Lively, *Seven Chemical Separations to Change the World*, Nature.

[4] P. J. J. Alvarez, C. K. Chan, M. Elimelech, N. J. Halas, and D. Villagrán, *Emerging Opportunities for Nanotechnology to Enhance Water Security*, Nat. Nanotechnol. 2018 138 **13**, 634 (2018).

[5] F. Fu and Q. Wang, *Removal of Heavy Metal Ions from Wastewaters : A Review*, J. Environ. Manage. **92**, 407 (2011).

[6] J. R. Werber, C. O. Osuji, and M. Elimelech, *Materials for Next-Generation Desalination and Water Purification Membranes*, Nat. Rev. Mater. **1**, (2016).

[7] A. Goyal, G. Marcandalli, V. A. Mints, and M. T. M. Koper, *Competition between CO_2 Reduction and Hydrogen Evolution on a Gold Electrode under Well-Defined Mass Transport Conditions*, J. Am. Chem. Soc. **142**, 4154 (2020).

[8] G. Segev et al., *The 2022 Solar Fuels Roadmap*, J. Phys. D. Appl. Phys. **55**, 323003 (2022).

[9] C. Xu, Q. Dai, L. Gaines, M. Hu, A. Tukker, and B. Steubing, *Future Material Demand for Automotive Lithium-Based Batteries*, Commun. Mater. **1**, 99 (2020).

[10] C. Liu, Y. Li, D. Lin, P.-C. Hsu, B. Liu, G. Yan, T. Wu, Y. Cui, and S. Chu, *Lithium Extraction from Seawater through Pulsed Electrochemical Intercalation*, Joule **4**, 1459 (2020).

[11] C. Tang, A. Yaroshchuk, and M. L. Bruening, *Flow through Negatively Charged, Nanoporous Membranes Separates Li+and K+due to Induced Electromigration*, Chem. Commun. **56**, 10954 (2020).

[12] J. A. Armstrong, E. E. L. Bernal, A. Yaroshchuk, and M. L. Bruening, *Separation of Ions Using Polyelectrolyte-Modified Nanoporous Track-Etched Membranes*, Langmuir **29**, 10287 (2013).

[13] A. E. Yaroshchuk, *Asymptotic Behaviour in the Pressure-Driven Separations of Ions of Different Mobilities in Charged Porous Membranes*, J. Memb. Sci. **167**, 163 (2000).

[14] A. E. Yaroshchuk, *Dielectric Exclusion of Ions from Membranes*, Advances in Colloid and Interface Science.

[15] A. E. Yaroshchuk, *Negative Rejection of Ions in Pressure-Driven Membrane Processes*, Adv. Colloid Interface Sci. **139**, 150 (2008).

[16] P. Hänggi and F. Marchesoni, *Artificial Brownian Motors: Controlling Transport on the Nanoscale*, Rev. Mod. Phys. **81**, 387 (2009).

[17] P. Reimann, *Brownian Motors: Noisy Transport Far from Equilibrium*, Phys. Rep. **361**, 57 (2002).

[18] B. Lau and O. Kedem, *Electron Ratchets: State of the Field and Future Challenges*, J. Chem. Phys. **152**, 200901 (2020).

[19] O. Kedem, B. Lau, and E. A. Weiss, *How to Drive a Flashing Electron Ratchet to Maximize Current*, Nano Lett. **17**, 5848 (2017).

[20] O. Kedem, B. Lau, and E. A. Weiss, *Mechanisms of Symmetry Breaking in a Multidimensional Flashing Particle Ratchet*, ACS Nano **11**, 7148 (2017).

[21] O. Andersson, J. Maas, G. Gelinck, and M. Kemerink, *Scalable Electronic Ratchet with Over 10% Rectification Efficiency*, Adv. Sci. **7**, (2020).

[22] P. Olbrich et al., *Terahertz Ratchet Effects in Graphene with a Lateral Superlattice*, Phys. Rev. B **93**, 1 (2016).

[23] P. Faltermeier, P. Olbrich, W. Probst, L.

Schell, T. Watanabe, S. A. Boubanga-Tombet, T. Otsuji, and S. D. Ganichev, *Helicity Sensitive Terahertz Radiation Detection by Dual-Grating-Gate High Electron Mobility Transistors*, J. Appl. Phys. **118**, 084301 (2015).

[24] M. Kabir, D. Unluer, L. Li, A. W. Ghosh, and M. R. Stan, *Electronic Ratchet : A Non-Equilibrium , Low Power*, 2011 11th IEEE Int. Conf. Nanotechnol. 482 (2011).

[25] O. Kedem, B. Lau, M. A. Ratner, and E. A. Weiss, *Light-Responsive Organic Flashing Electron Ratchet*, Proc. Natl. Acad. Sci. **114**, 8698 (2017).

[26] T. Tanaka, Y. Nakano, and S. Kasai, *GaAs-Based Nanowire Devices with Multiple Asymmetric Gates for Electrical Brownian Ratchets*, Jpn. J. Appl. Phys. **52**, (2013).

[27] H. Linke, T. E. Humphrey, A. Löfgren, A. O. Sushkov, R. Newbury, R. P. Taylor, and P. Omling, *Experimental Tunneling Ratchets*, Science (80-.). **286**, 2314 (1999).

[28] O. V. Mikhnenko, S. D. Collins, and T. Q. Nguyen, *Rectifying Electrical Noise with an Ionic-Organic Ratchet*, Adv. Mater. **27**, 2007 (2015).

[29] Y. Hu, V. Brus, W. Cao, K. Liao, H. Phan, M. Wang, K. Banerjee, G. C. Bazan, and T. Q. Nguyen, *Understanding the Device Physics in Polymer-Based Ionic-Organic Ratchets*, Adv. Mater. **29**, (2017).

[30] S. Hubmann, V. V Bel'kov, L. E. Golub, V. Y. Kachorovskii, M. Drienovsky, J. Eroms, D. Weiss, and S. D. Ganichev, *Giant Ratchet Magneto-Photocurrent in Graphene Lateral Superlattices*, Phys. Rev. Res. **2**, 33186 (2020).

[31] E. M. Roeling, W. C. Germs, B. Smalbrugge, E. J. Geluk, T. De Vries, R. A. J. Janssen, and M. Kemerink, *Organic Electronic Ratchets Doing Work*, Nat. Mater. **10**, 51 (2011).

[32] E. M. Roeling, W. C. Germs, B. Smalbrugge, E. J. Geluk, T. De Vries, R. A. J. Janssen, and M. Kemerink, *The Performance of Organic Electronic Ratchets*, AIP Adv. **2**, (2012).

[33] S. Marbach and L. Bocquet, *Active Sieving across Driven Nanopores for Tunable Selectivity*, J. Chem. Phys. **147**, (2017).

[34] S. Marbach, N. Kavokine, and L. Bocquet, *Resonant Osmosis across Active Switchable Membranes*, J. Chem. Phys. **152**, (2020).

[35] J. M. R. Parrondo, J. M. Blanco, F. J. Cao, and R. Brito, *Efficiency of Brownian Motors*, Europhys. Lett. **43**, 248 (1998).

[36] R. Nouri and W. Guan, *Nanofluidic Charged-Coupled Devices for Controlled DNA Transport and Separation*, Nanotechnology **32**, 345501 (2021).

[37] S. Ardo, G. Segev, F. M. Toma, J. W. Ager, R. Kautz, and D. M. Larson, *Ratchet-Based Ion Pumping Membrane Systems.*, US20200402782A1 (2020).

[38] V. M. Rozenbaum, T. Y. Korochkova, A. A. Chernova, and M. L. Dekhtyar, *Brownian Motor with Competing Spatial and Temporal Asymmetry of Potential Energy*, Phys. Rev. E - Stat. Nonlinear, Soft Matter Phys. **83**, 1 (2011).

[39] M. S. Kodaimati, O. Kedem, G. C. Schatz, and E. A. Weiss, *Empirical Mappings of the Frequency Response of an Electron Ratchet to the Characteristics of the Polymer Transport Layer*, J. Phys. Chem. C **123**, 22050 (2019).

[40] M. J. Skaug, C. Schwemmer, S. Fringes, C. D. Rawlings, and A. W. Knoll, *Nanofluidic Rocking Brownian Motors*, Science (80-.). **359**, 1505 (2018).

[41] C. Schwemmer, S. Fringes, U. Duerig, Y. K. Ryu, and A. W. Knoll, *Experimental Observation of Current Reversal in a Rocking Brownian Motor*, Phys. Rev. Lett. **121**, 104102 (2018).

[42] Q. Chen, B. Q. Ai, and J. W. Xiong, *Brownian Transport of Finite Size Particles in a Periodic Channel Coexisting with an Energetic Potential*, Chaos **24**, (2014).

[43] A. Słapik, J. Łuczka, P. Hänggi, and J. Spiechowicz, *Tunable Mass Separation via Negative Mobility*, Physical Review Letters.

[44] T. Motz, G. Schmid, P. Hänggi, D. Reguera, and J. M. Rubí, *Optimizing the Performance of the Entropic Splitter for Particle Separation*, J. Chem. Phys. **141**, 074104 (2014).

[45] D. Reguera, A. Luque, P. S. Burada, G. Schmid, J. M. Rubí, and P. Hänggi, *Entropic Splitter for Particle Separation*, Phys. Rev. Lett. **108**, 1 (2012).

[46] B. Yang, F. Long, and D. C. Mei, *Negative Mobility and Multiple Current Reversals Induced by Colored Thermal Fluctuation in an Asymmetric Periodic Potential*, Eur. Phys. J. B **85**, 2 (2012).

[47] P. Nicollier, C. Schwemmer, F. Ruggeri, D. Widmer, X. Ma, and A. W. Knoll,

Nanometer-Scale-Resolution Multichannel Separation of Spherical Particles in a Rocking Ratchet with Increasing Barrier Heights, Phys. Rev. Appl. **15**, 034006 (2021).

[48] V. M. Rozenbaum, I. V. Shapochkina, Y. Teranishi, and L. I. Trakhtenberg, *Symmetry of Deterministic Ratchets*, Phys. Rev. E **100**, 22115 (2019).

[49] V. M. Rozenbaum, *High-Temperature Brownian Motors: Deterministic and Stochastic Fluctuations of a Periodic Potential*, JETP Lett. **88**, 342 (2008).

[50] T. Luo, S. Abdu, and M. Wessling, *Selectivity of Ion Exchange Membranes: A Review*, J. Memb. Sci. **555**, 429 (2018).

[51] T. Sata, *Studies on Anion Exchange Membranes Having Permselectivity for Specific Anions in Electrodialysis — Effect of Hydrophilicity of Anion Exchange Membranes on Permselectivity of Anions*, **167**, 1 (2000).

[52] T. Sata, T. Sata, and W. Yang, *Studies on Cation-Exchange Membranes Having Permselectivity between Cations in Electrodialysis*, **206**, 31 (2002).

[53] T. Luo, F. Roghmans, and M. Wessling, *Ion Mobility and Partition Determine the Counter-Ion Selectivity of Ion Exchange Membranes*, J. Memb. Sci. **597**, 117645 (2020).

[54] E. T. Acar, S. F. Buchsbaum, C. Combs, F. Fornasiero, and Z. S. Siwy, *Biomimetic Potassium-Selective Nanopores*, 1 (2019).

[55] X. Li et al., *Fast and Selective Fluoride Ion Conduction in Sub-1-Nanometer Metal-Organic Framework Channels*, Nat. Commun. **10**, 1 (2019).

[56] S. Yang, F. Zhang, H. Ding, and P. He, *Lithium Metal Extraction from Seawater*, Joule **2**, 1648 (2018).

[57] B. Swain, *Recovery and Recycling of Lithium : A Review*, Sep. Purif. Technol. **172**, 388 (2017).

[58] J. Rabinowitz, C. Cohen, and K. L. Shepard, *An Electrically Actuated, Carbon-Nanotube-Based Biomimetic Ion Pump*, Nano Lett. **20**, 1148 (2020).

[59] S. Kim, E. I. Ozalp, and J. A. Weldon, *Stacked Gated Nanofluidic Logic Gate Membrane*, IEEE Trans. Nanotechnol. **18**, 536 (2019).

[60] S. Kim, E. I. Ozalp, M. Darwish, and J. A. Weldon, *Electrically Gated Nanoporous Membranes for Smart Molecular Flow Control*, Nanoscale **10**, 20740 (2018).

[61] T. Cebeci and P. Bradshaw, *Physical and Computational Aspects of Convective Heat Transfer* (Springer, New York, NY, 1988).

[62] F. Harnisch and U. Schrçder, *Selectivity versus Mobility : Separation of Anode and Cathode in Microbial Bioelectrochemical Systems*, 921 (2009).